*J. Fluid Mech.* (2006), *vol.* 559, *pp.* 81–106.  
doi:10.1017/S0022112006009918 Printed in the United Kingdom

# Topographically controlled, breaking-wave-induced macrovortices. Part 3. The mixing features

By A. PIATTELLA[1], M. BROCCHINI[2] AND A. MANCINELLI[1]

[1]Istituto di Idraulica e Infrastrutture Viarie, Università Politecnica delle Marche, Via Brecce Bianche, 60131, Ancona, Italy

[2]DIAM, Università di Genova, via Montallegro 1, 16145 Genova, Italy

(Received 16 March 2005 and in revised form 7 December 2005)

The series of papers on the flow dynamics due to wave-induced macrovortices is completed with a statistical analysis of the mixing of the shallow flows occurring around submerged structures used for coastal protection. This is investigated with specific focus on the role played by large-scale horizontal eddies shed in coastal areas by waves breaking corresponding to topographic features like submerged breakwaters. As in Part 2, conditions due to isolated or arrays of breakwaters are studied. Analysis of particle statistics is used to determine both the features of the induced quasi-two-dimensional flow and to derive general properties. In particular three distinct regimes are found to characterize the flow evolution. Asymptotic regimes for small and large times share in any of the features of typical 'ballistic' and 'Brownian' regimes. Focus is mainly placed on properties of the 'intermediate time' regime which are seen to depend on the chosen topographic configuration. In agreement with the deterministic results of Part 2, we find that, because of an intense longshore current, an isolated breakwater induces a larger dispersion than that due to an array of breakwaters, characterized by a rip current. Moreover, for the same topography, the diffusivity grows with the local wavelength. Comparison with field data suggests that results of scaled-down laboratory experiments reproduce well natural mixing conditions. A simple formulation of absolute diffusivity, to be used in practical applications related to environmental quality management, is, finally, proposed.

## 1. Introduction

In many cases shallow-water flows, in which the horizontal scales are much larger than the vertical scale, are characterized by the presence of large-scale features similar to those of two-dimensional turbulence. Such flows are most often analysed in terms of depth-averaged properties as in the case of the classic nonlinear shallow water equation (NSWE). The importance for shallow flows of horizontal large-scale eddies (macrovortices hereinafter) has been widely reported for coastal flows (e.g. Oltman-Shay, Howd & Berkemeier 1989; Peregrine 1998; Chen *et al.* 1999; Brocchini *et al.* 2002).

Large-scale horizontal mixing of coastal flows is greatly promoted by macrovortices which are generated because of a spatially non-uniform breaking of the incoming waves (e.g. Peregrine 1998; and Part 1 of this series, Brocchini *et al.* 2004). Although such differential breaking may be induced for various reasons (irregularity of the

incoming field, wave–wave interaction, etc.) the major cause of persistent breaking unevenness is due to topography. This is often characterized by longshore isolated (natural bumps or manmade submerged breakwaters) or almost-continuous features (bars or arrays of submerged breakwaters) over which uniform wave fronts break with large lateral gradients. Hence, macrovortices can be shed which alter both the hydrodynamics and the morphodynamics (Steijn *et al.* 1998; Chen *et al.* 1999; Part 1).

In particular the companion papers, Part 1 (Brocchini *et al.* 2004) and Part 2 (Kennedy *et al.* 2006), analyse experimentally, computationally and analytically the behaviour of breaking-wave-induced macrovortices during startup conditions. Part 1 examines the generation mechanisms and general hydrodynamic behaviour of isolated breakwaters, with particular attention paid to vortex trajectories and shedding periods, while Part 2 analyses the transition of startup macrovortices from single breakwaters to rip current topographies using computations and laboratory experiments. Both studies provide insight into the fundamental deterministic features of macrovortex evolution.

The present work aims to complete the analysis by characterizing the mixing features of macrovortices in terms of the statistical properties of the flow they induce, in conjunction with waves, in the nearshore region. In fact the role of macrovortices is also fundamental to any water quality evaluation of coastal areas. In most cases the evolution of passive tracers, like non-reactive pollutants, is predicted by means of depth-averaged convection–diffusion equations of the type

$$\frac{\partial C}{\partial t} = -\boldsymbol{v}\cdot\nabla C + \nabla\cdot(\boldsymbol{K}\cdot\nabla C) \tag{1.1}$$

where $C$ is the tracer concentration, $\boldsymbol{v}$ is the vector of the depth-averaged velocity and $\boldsymbol{K}$ is the depth-averaged diffusivity tensor (e.g. Taylor 1921). This equation can only be solved for $C$ if, beyond the flow field, the diffusivity is known through a constitutive relationship of Fickian type. Such a closure is largely dominated by the presence of large-scale coherent features like macrovortices and is typical of the flow conditions at hand. Examples of closures for coastal flows can be found in Inman, Tait & Nordstrom (1971), Larson & Kraus (1991) and Takewaka, Misaki & Nakamura (2003).

Results from recent experimental studies of shallow-water turbulence suggest that such turbulence, generated in shallow jets (Dracos, Giger & Jirka 1992), wakes (Chen & Jirka 1995) and mixing layers (Uijttewaal & Booij 2000), is characterized by spectral properties typical of two-dimensional turbulence. In other words both a direct enstrophy cascade at large wavenumbers and an inverse energy cascade at small wavenumbers are evident, with decay rates typical of two-dimensional turbulence i.e. the '$-5/3$ law' and '$-3$ law' respectively for energy and enstrophy cascading (Kraichnan 1967). In this respect it is also desirable to model the transport properties of shallow-water macrovortices in analogy to those due to coherent barotropic vortices of two-dimensional turbulence (Provenzale 1999).

In a two-dimensional turbulent flow characterized by large-scale coherent structures the evolution of tracers and the flow dynamics are so intimately connected that knowledge of the former may give a predictive key for the latter, and vice versa. This approach, which has been usefully employed to investigate atmospheric (e.g. Richardson 1926; Er-El & Peskin 1981) and oceanic (e.g. LaCasce & Bower 2000; LaCasce & Ohlmann 2003) flows, is now also becoming of interest for nearshore dynamics (Fong & Stacey 2003). This is also connected with the recent developments in the monitoring of coastal waters by means of video techniques (e.g. Lippmann & Holman 1989). With such equipment floats/dye released near the shore can be

monitored for times/areas large enough to provide the fundamental data for any dispersion analysis. For example, the recent work of Takewaka *et al.* (2003) shows how it is possible to apply this approach to compute dispersive parameters of dye patches released near the breaking region. With this perspective, and with the aim of using information from prototype-scale and laboratory-scale experiments, we attempt to create a theoretical framework for the interpretation of statistics of tracers released in coastal areas.

In § 2 we give a broad overview of the generation mechanism for macrovortices in the presence of topographic gradients (§ 2.1) and of the theoretical background used for the statistical analysis of Lagrangian dispersion (§ 2.2). In § 3 we describe the main features of the experimental tests used to determine the mixing properties associated with the presence of currents, waves and macrovortices and we briefly describe the main results of the hydrodynamic analysis. In § 4 we illustrate the main findings of the analysis of passive tracer trajectories. Moreover, we describe comparisons to prototype-scale experiments and give a quantitative formulation for eddy diffusivity to be used in coastal mixing computations. Section 5 summarizes the main results and concludes the work.

## 2. Theoretical background

### 2.1. *Topographic-induced generation of macrovortices in coastal environments*

In this section we briefly illustrate the mechanism of generation of vorticity or, better, potential vorticity in the NSWE framework.

In the pseudo-inviscid NSWE framework (Schär & Smith 1993) in the absence of shock-type solutions no generation of either vorticity $\omega$, defined as $\omega \equiv v_x - u_y$, or potential vorticity, $\Omega \equiv \omega/d$, occurs. (In the above the symbol $(\cdot)_i$ represents partial differentiation with respect to the generic variable $i$, $d$ is the total water depth and $\boldsymbol{v} = (u, v)$ the vector of the depth-averaged velocity.) In particular $\omega$ can only be transported or locally intensified/reduced if the total depth $d$ increases/decreases when following a 'water column' which represents a coherent body of water of constant volume; following the same water column the potential vorticity $\Omega$ is conserved.

However, if shocks are present in the domain, jump conditions, also known as Rankine–Hugoniot conditions, hold across the discontinuity. These conditions introduce a generation mechanism of vorticity/potential vorticity not accounted for in the absence of shocks. In particular if dissipative body forces, typically due to bores or hydraulic jumps (i.e. shocks), are accounted for, potential vorticity, generated by shocks, moves inside the fluid body with the water columns (e.g. Bühler & Jacobson 2001).

Following the approach of Pratt (1983) we assume, for simplicity, that a shock with a straight, finite front propagates at velocity $V$ in the $x$-direction (a simple rotation allows the following to be generalized to any shock incidence). If points with coordinates $x_A$ and $x_B$ lie respectively upstream and downstream of the shock there is a jump in $\Omega$ across the shock:

$$[\Omega]_{x_A}^{x_B} = -\left[\frac{2}{g[d(x_A) + d(x_B)]d(x_A)d(x_B)}\right]^{1/2} \frac{\partial \widehat{E}_D}{\partial y} \tag{2.1}$$

with

$$\widehat{E}_D = \frac{[d(x_B) - d(x_A)]^3}{4d(x_A)d(x_B)}, \quad [\Omega]_{x_A}^{x_B} \equiv \Omega(x_B) - \Omega(x_A). \tag{2.2}$$

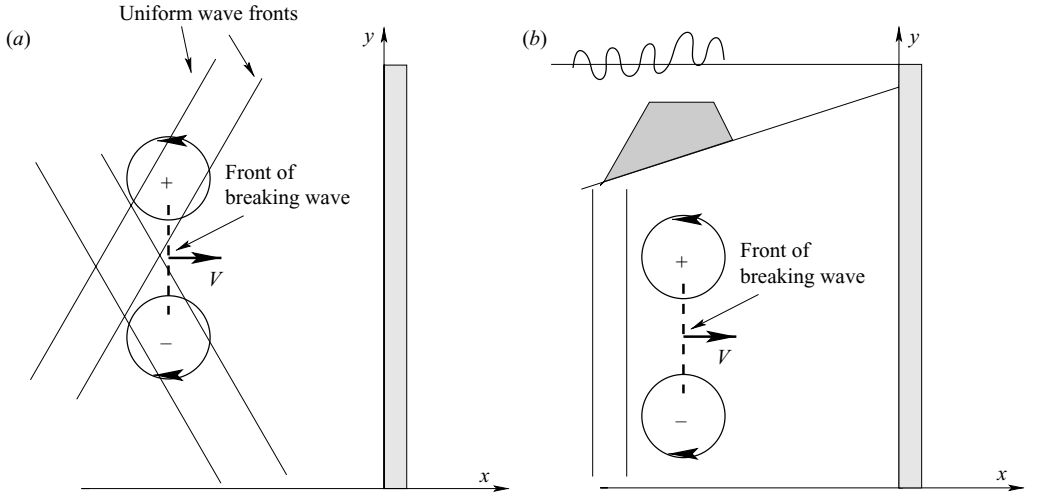


FIGURE 1. The generation of breakers of finite length: (*a*) uniform wave fronts propagating at an angle over a uniform beach and (*b*) uniform wave fronts passing over a submerged breakwater and breaking locally. Circles and arrows give a schematic representation of the flow rotation at the edges of the breaker. (Adapted from Brocchini *et al.* 2002.)

Note that $\widehat{E}_D$, being the specific (per unit weight) energy dissipation rate occurring at a steady (hydraulic jump) or moving (bore) flow discontinuity, relates to $E_D$ of Part 1 as $\widehat{E}_D = E_D/g$. Hence, potential vorticity is generated at locations where there is a cross-flow variation of $\widehat{E}_D$. Clearly this is maximum where there is an abrupt cross-flow change of $[d]_{x_A}^{x_B}$. Also note that the sign of vorticity generated is opposite to the sign of $\partial[d(x_B) - d(x_A)]/\partial y$.

The above generation mechanism can be applied to a number of nearshore flow conditions in which breakers of finite longshore length are present, having been originated under various circumstances (e.g. Peregrine 1998; Brocchini *et al.* 2002). Two examples are reported in figure 1 which are of considerable importance for nearshore circulation. The first (figure 1*a*) illustrates the case in which uniform wave fronts propagate towards the shoreline over a uniformly sloping beach. Their interaction can lead to local steepening and breaking so that a breaker of finite longshore length is generated. At the edges of such a breaker, potential vorticity is generated due to the large value of $\partial[d(x_B) - d(x_A)]/\partial y$. For a more exhaustive analysis of the generation of vorticity by breakers of finite length we refer the reader to Peregrine (1998). The second case (figure 1*b*) is of greater practical importance as it models the flow conditions generated by waves approaching the shore and locally breaking over a submerged breakwater. (Knowledge of these modalities of mixing, similar to those occurring at a natural bar, is fundamental in assessing water quality properties at coasts close to urban/tourist areas.) Vorticity generation at the edges of a submerged breakwater and the evolution of macrovortices in the nearshore has been investigated experimentally and numerically in great detail (Brocchini *et al.* 2002; Part 1 and Part 2).

### 2.2. *Lagrangian dispersion*

In this section we summarize some fundamental results on absolute and relative dispersion of passive tracers, the main assumption being that Lagrangian drifters are passively advected in a two-dimensional flow. Because of the close dependence of

mixing (particle separation $D$) on the flow (spectral energy density $E(k)$) and vice versa, mixing properties are often used to indirectly characterize the flow. Hence, mixing statistics are used here for the interpretation, in strict analogy with the works of LaCasce & Bower (2000) and LaCasce & Ohlmann (2003), of the flow mixing observed in the experiments described in § 3.

In particular we compute the absolute dispersion defined as

$$\left\langle X_{ij}^2(t)\right\rangle \equiv \frac{1}{M}\sum_{particles} x_i(t)x_j(t) \tag{2.3}$$

where $x_i$ is the particle displacement from its initial position in the $x$-direction ($i, j = 1$) and in the $y$-direction ($i, j = 2$) and $M$ is the number of particles. The trace of this matrix is the 'total' absolute dispersion, i.e. $\langle X^2\rangle = \langle X_{11}^2\rangle + \langle X_{22}^2\rangle = \langle X_x^2\rangle + \langle X_y^2\rangle$. The absolute diffusivity, i.e. the time derivative of the absolute dispersion, is

$$K^{(1)} \equiv \frac{1}{2}\frac{\mathrm{d}}{\mathrm{d}t}\langle X^2\rangle. \tag{2.4}$$

We can also compute the relative dispersion tensor as

$$\left\langle D_{ij}^2(t)\right\rangle \equiv \frac{1}{N}\sum_{pairs} y_i(t)y_j(t) \tag{2.5}$$

where $y_i$ is the particles' separation in the $x$-direction ($i, j = 1$) and in the $y$-direction ($i, j = 2$) and $N$ is the number of pairs. In this case we have to identify pairs of particles. A pair is taken to be any two particles (or passive tracers) which come within a predefined distance apart at a given time. Different maximum separations are used for identifying pairs. Usually, the smaller the maximum initial separation, the greater the range of scales sampled, but also smaller the sample size. The rate of separation between the particles often depends on the initial separation $D_0$.

As for the absolute dispersion, the trace of this matrix is the 'total' relative dispersion, i.e. $\langle D^2\rangle = \langle D_{11}^2\rangle + \langle D_{22}^2\rangle = \langle D_x^2\rangle + \langle D_y^2\rangle$ and we can define the relative diffusivity as the time derivative of the dispersion

$$K^{(2)} \equiv \frac{1}{2}\frac{\mathrm{d}}{\mathrm{d}t}\langle D^2\rangle. \tag{2.6}$$

2.2.1. *Absolute properties of mixing*

Particle (floaters in the experiments) data are most often analysed in terms of absolute statistics, since the relative ones are harder to predict and much less familiar in the oceanic and coastal context. However, fluid dynamicists recently recognized the importance of analysing the physics at different scales by means of both absolute and relative statistics (e.g. LaCasce & Bower 2000).

Flow regimes, in a description which makes use of absolute statistics, are usually separated with the use of suitable time scales like, for example, the Lagrangian decorrelation time $T_L$, which is defined as

$$T_L \equiv \int_0^\infty R(t)\,\mathrm{d}t \tag{2.7}$$

and in which $R(t)$ is the normalized Lagrangian autocorrelation function. Note that, because of (2.7) and since $R(t) \to 0$ for $t \to \infty$, $T_L$ can be interpreted as the time necessary for each particle to lose its memory of its initial velocity.

If absolute statistics are used, the natural definition for the 'ballistic regime' is $t \ll T_L$ (Taylor 1921). In this regime the absolute dispersion typically increases quadratically in time while the absolute diffusivity undergoes a linear growth

$$\langle X^2 \rangle \propto t^2, \quad K^{(1)} \propto t. \tag{2.8}$$

Once the 'Brownian regime' is reached, i.e. for $t > T_L$, the absolute dispersion increases linearly in time, determining a constant diffusivity $K^{(1)} \to$ const. Ultimately, particles' separations reach the scale of the energy-containing eddies $L_L$ and the individual particle velocities become uncorrelated ($L_L$ is also known as the decorrelation length scale).

The theoretical behaviour of the absolute dispersion based on Taylor's theory has been systematically observed for non-homogeneous oceanic and atmospheric velocity fields (LaCasce & Bower 2000); hence the asymptotic behaviour of the absolute dispersion is disconnected from the restrictive hypothesis of homogeneity.

Usually the absolute dispersion and diffusivity are used to model the dynamics for times sufficiently large that the anisotropic large-scale turbulence, whose main effect is convecting the clouds of passive tracers, is greater than the small-scale turbulence. Vice versa, for small times the isotropic small-scale turbulence is more important and its main effect is to deform the cloud of passive tracers rather than to advect it. This suggests that the absolute dispersion is more appropriate for large times/lengths and the relative dispersion for small times/lengths.

### 2.2.2. *Relative properties of mixing*

The definition of 'small times' depends on the approach used to analyse the mixing. If relative statistics are to be analysed a more restrictive definition of the 'small time regime' should be used which makes use of $T_p$. This is the time at which, soon after deployment, pairs of particles have lost memory of their initial separation $D_0$, and, for this reason, $T_p$ is smaller than $T_L$. Since $T_p$ depends on the particles' initial separation the 'large-time' limit cannot be uniquely defined and it makes more sense to think in terms of a large-space limit. This is defined as the size of the energy-containing eddies.

Hence for small separations a behaviour similar to the ballistic regime is observed for which

$$\langle D^2 \rangle \propto t^2 \quad \text{and} \quad K^{(2)} \propto t. \tag{2.9}$$

while for separations larger than $L_L$ the particles are uncorrelated and the relative dispersion becomes absolute with a Brownian regime described by

$$K^{(2)} \approx 2K^{(1)}, \tag{2.10}$$

for which the relative diffusivity $K^{(2)}$ is constant and approximately equal to twice the absolute diffusivity $K^{(1)}$.

### 2.2.3. *The intermediate regimes: anomalous diffusion*

In the intermediate regime, various behaviours can be observed depending on the evolution modalities of large-scale coherent vortices. For example, Elhmaidi, Provenzale & Babiano (1993) report two different 'anomalous' absolute dispersion laws, depending on whether it is a flow in which deformation dominates rotation ($\langle X^2 \rangle \propto t^{5/4}$) or vice versa ($\langle X^2 \rangle \propto t^{5/3}$).

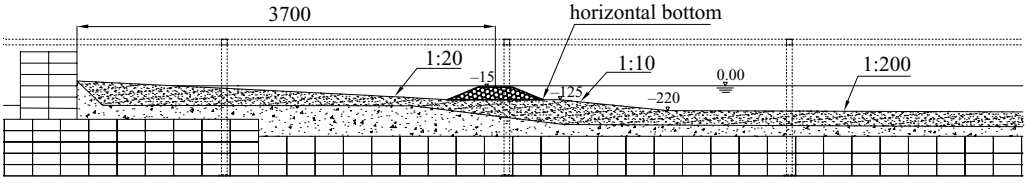


FIGURE 2. Cross-shore section of the Bari experimental set-up, corresponding to the submerged breakwater.

Differences can also be found for the relative dispersion:

(i) In the case of a dominance of enstrophy cascade an exponential growth of particle separations and, consequently, a $D^2$-law in the relative diffusivity are observed:

$$\langle D^2 \rangle \propto \exp\left(\beta^{1/3} t\right) \quad \text{and} \quad K^{(2)} \propto \beta^{2/3} \langle D^2 \rangle \tag{2.11}$$

in which $\beta$ represents the flux of enstrophy injected at the forcing wavenumber. The behaviour described by (2.11) was seen to characterize the experimental data of Morel & Larcheveque (1974) and Er-El & Peskin (1981) for atmospheric mixing and of LaCasce & Ohlmann (2003) for oceanic mixing;

(ii) On the other hand, in the presence of a background shear (Bowden 1965; Bennett 1987), the turbulent diffusivity follows a 4/3-law. For particles pairs taking independent random walks in the $y$-direction in the presence of a shear flow ($\mathrm{d}U/\mathrm{d}y$) in the $x$-direction, Bennett (1987) found that the dispersion in the $x$-direction is characterized by a $t^3$ growth, accompanied by a $D^{4/3}$ growth of the diffusivity in the $x$-direction:

$$\left\langle D_x^2 \right\rangle \propto t^3 \quad \text{and} \quad K_x^{(2)} \propto \left\langle D^{4/3} \right\rangle. \tag{2.12}$$

Similar behaviour can also occur in the presence of waves. A group of particles advected by monochromatic waves only exhibits a quadratic-in-time dispersion in the direction of the wave phase speed, for example in the $x$-direction (LaCasce & Speer 1999). However, with a transversal mixing superimposed, the dispersion in the $x$-direction can grow as $t^3$ as in the case of a simple shear (LaCasce & Bower 2000).

## 3. The laboratory experiments

We study the evolution of macrovortices generated during a large-scale laboratory experiment in terms of the statistical properties of passive tracers. This analysis, specifically designed to evaluate the features of the mixing induced by both single breakwaters and rip-channel configurations, is, in spirit, very similar to that performed to study the mixing features of oceanic eddies by LaCasce & Bower (2000). The advantage of the present analysis is the possibility of strictly controlling and, eventually, repeating the input flow conditions.

The experiments, described in detail in Lorenzoni *et al.* (2004, 2005), were carried out in a 40 m × 29 m portion of the large-scale wave basin of the Polythecnic of Bari (90 m long, 50 m wide). Model breakwaters (4 m long, with berm width of about 0.3 m and constant submergence of about 0.015 m) were placed over a sandy beach of almost uniform slope both offshore of the breakwaters (1:200) and inshore of them (1:20) (see figure 2). Fine sand ($d_{50} = 0.2$ mm) was used to cover the bottom. At the offshore boundary of the domain, with still-water depth of 0.79 m, both regular and irregular waves were generated with periods in the range 0.91–1.82 s and heights in the range 1.67–6.67 cm. All these conditions are compatible with a Froude similarity of prototype conditions scaled-down at a length ratio of 1:30.

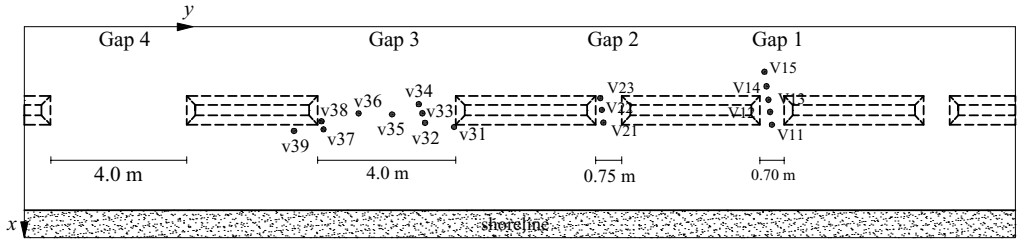


FIGURE 3. Planimetric layout of the Bari experimental set-up and locations of the ADVs (labelled V).

| $L_{t-rip}$ (m) | $L_{t-single}$ (m) | $L_c$ (m) | $h_b$ (m) | $s$ |
|---|---|---|---|---|
| 0.75 | 4.00/5.40 | 4.00 | 0.125 | 0.005 |

TABLE 1. Main geometrical characteristics of the experimental tests.

### 3.1. *The flow evolution*

Two distinct configurations were analysed (see figure 3, in which the locations of the acoustic Doppler velocimeters (ADVs) are also shown). In the single breakwater configuration the structure considered is far from any other structure (left-hand side of figure 3) while in the rip current configuration the submerged breakwaters were separated by narrow gaps (right-hand side of figure 3). Table 1 summarizes the main geometrical characteristics of these two configurations. Using the notation of Part 2, we define $L_t$ the size of the gap between contiguous breakwaters and $L_c$ the breakwater crest size; $h_b$ is the still-water depth at the toe of the breakwaters while $s$ is the beach slope.

In all cases velocities around the breakwaters and water levels over the breakwaters were measured (see Lorenzoni *et al.* (2005) for more details). The spatial distribution of the structures is very similar to that of Part 2. The main differences between this experimental configuration and that of Part 2 is the presence of the mobile sand bed. This allows for natural morphodynamic evolution to occur, hence closely reproducing hydrodynamic and mixing field conditions.

The general flow evolution is similar to that observed in previous similar studies (Haller, Dalrymple & Svendsen 2002; Dronen *et al.* 2002). Waves propagating normally to the beach over the described topography determine a flow characterized by both longshore and rip currents, which make up the so-called circulation cells of the primary circulation. The latter is determined by differential wave breaking since waves break over the submerged breakwaters and produce a cross-shore setup of the water surface. The setup is less pronounced in the rip channel, in which the interaction with the seaward-flowing rip current modifies the approaching waves. Waves flowing to the shore directly through the rip channel induce finite-length breakers very close to the shore and, consequently, a pair of macrovortices which rotate oppositely to the bar vortices (vortices [1] and [2] of Part 2) of the primary circulation. These are the shore vortices [4] described in Part 2 and partially responsible, along with self-advection, for the longshore motion of the bar vortices.

More details on specific features of breaking can be found in Lorenzoni *et al.* (2005). For the purposes at hand it is sufficient to recall the major difference in behaviour between long and short waves: they both break around the seaward toe of the

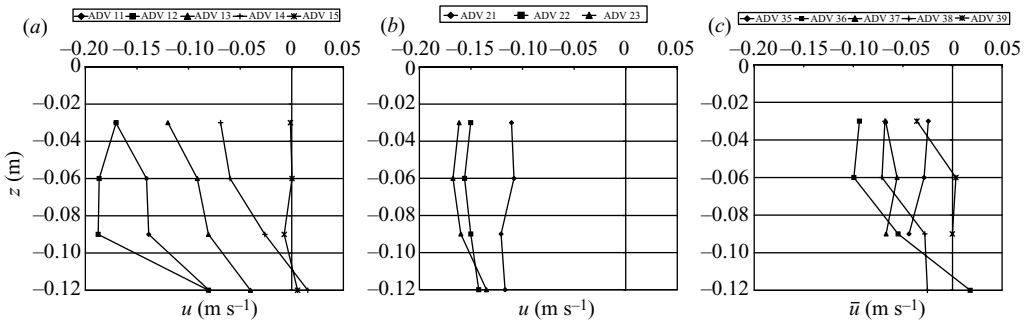


FIGURE 4. Vertical distribution of the time-averaged cross-shore velocity $\overline{u}$: (*a*) gap 1, (*b*) gap 2 and (*c*) gap 3. (Adapted from Lorenzoni *et al.* 2004.)

| Cases | $H_0^m$ (cm) | $T_0^m$ (s) | $H_0^p$ (m) | $T_0^p$ (s) | $I_{r0}$ |
|---|---|---|---|---|---|
| bari_a | 1.67 | 0.9 | 0.5 | 5 | 0.043 |
| bari_b | 1.67 | 1.8 | 0.5 | 10 | 0.079 |
| bari_c | 3.33 | 0.9 | 1.0 | 5 | 0.031 |
| bari_d | 3.33 | 1.8 | 1.0 | 10 | 0.056 |
| bari_e | 5.00 | 0.9 | 1.5 | 5 | 0.025 |
| bari_f | 5.00 | 1.8 | 1.5 | 10 | 0.046 |
| bari_g | 6.67 | 0.9 | 2.0 | 5 | 0.022 |
| bari_h | 6.67 | 1.8 | 2.0 | 10 | 0.040 |
| bari_j (irregular) | 5.00 | 1.8 | 1.5 | 10 | 0.046 |

TABLE 2. Main characteristics of the experimental cases performed at the University of Bari. $H_0$, $T_0$ and $I_{r0}$ are respectively the offshore wave height, period and corresponding Iribarren number (model offshore water depth of 0.79 m), where superscripts $m$ and $p$ refer to the model and prototype scales, respectively.

structures but the former as shallow-water bores and the latter as intermediate-water spillers.

Rip currents are often unstable, with velocities larger in the middle of the gap and decreasing seaward, also due to the waves' action. The large velocities generated within the rip channel induce intense localized erosion and offshore sand transport.

This is confirmed, for example, by figure 4 in which the experimental vertical distribution of cross-shore, time-averaged velocities $\overline{u}$ are shown. These refer to the test characterized by a regular waves of height $H_0^m = 5$ cm and period $T_0^m = 1.8$ s (bari_f of table 2). The velocities were measured once the flow pattern reached a quasi-steady state for an period of 30 s and with a sampling frequency equal to 20 Hz. In particular, velocities towards the offshore reach the maximum values of about $\overline{u} = -0.19\,\mathrm{m\,s^{-1}}$ at the inshore middle of the gap, both for gap 1 and gap 2, and become almost vanishing within a cross-shore distance of about 4–5 gap widths. This seems to confirm the numerical results of Mancinelli *et al.* (2001), in which the rip currents are locally intensified near the breakwater but made spatially unstable by the presence of macrovortices generated by the depth gradients at the ends of the submerged breakwaters ('local circulation'). On the contrary, numerical simulations of Part 1 show that in the case of isolated breakwaters macrovortices slowly propagating towards the shoreline become one of the most important means of forcing, together with the waves, of the general circulation. For the single breakwater configuration

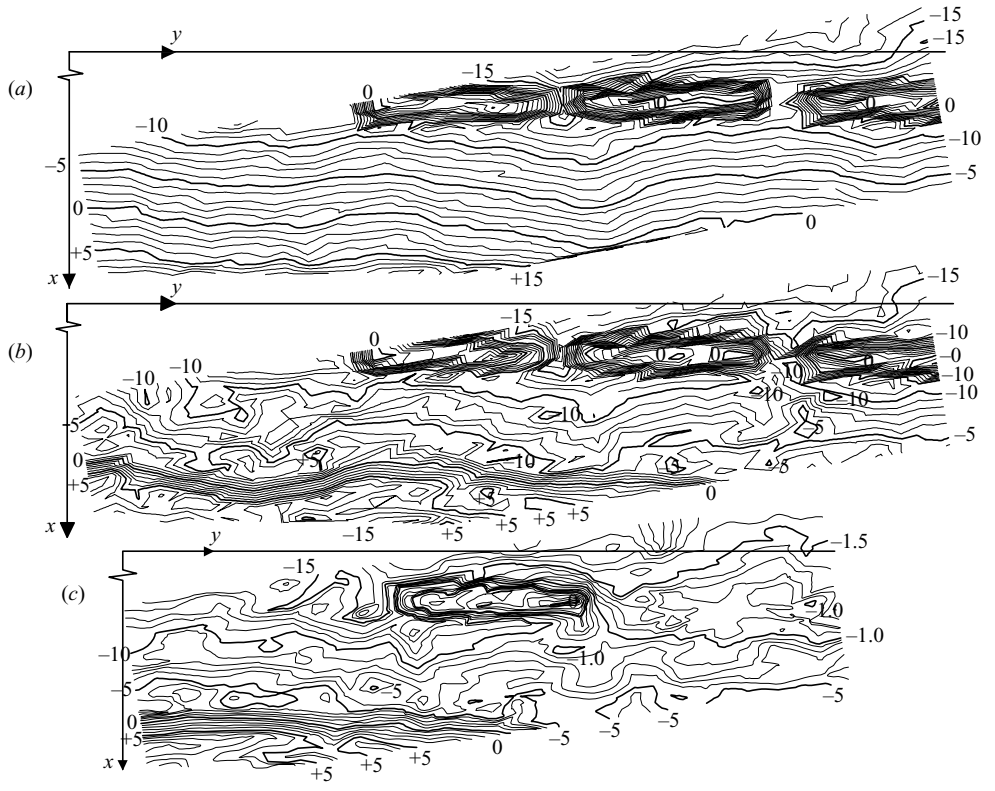


FIGURE 5. Bathymetry for the rip current configuration (*a*) at the beginning of the experimental tests and (*b*) after about 15 hours of run. (*c*) Bathymetry used for the mixing analysis for the single breakwater configuration. Bathymetric data were obtained by means of a touch-sensitive two-dimensional bed profiler.

(see figure 4*c*) the cross-shore velocities are less intense (approximately one third) than those characteristic of the rip current configuration.

In general the vertical velocity profiles are all characterized by weak gradients. An exception seems to be the profiles measured at the middle of the gap. There the surface water seems to flow offshore more rapidly than the lower water mass, hence giving a relatively large vertical velocity gradient at the gap. In all cases the largest velocity is attained at the surface. These observations are partially at odds with those of Haas & Svendsen (2002) who found the profile of the rip current to have the largest vertical gradients offshore of the gap, being almost uniform within the gap. This discrepancy seems to be mainly due to the fundamental difference in the bottom configuration of the two experiments: in the Bari experiments the sandy bed is prone to erosion/deposition with consequent large variations of the local water depth, as shown in figure 5.

### 3.2. *Data collection for the mixing analyses*

After around 15 hours of run, i.e. once the bathymetry has reached the quasi-steady state of figure 5(*b*), the analysis of the mixing induced by a rip current configuration started.

Floaters (10–25 wooden spheres with diameters of 25–42 mm) were released around the breakwaters and their meandering tracked with a fixed videocamera. The initial

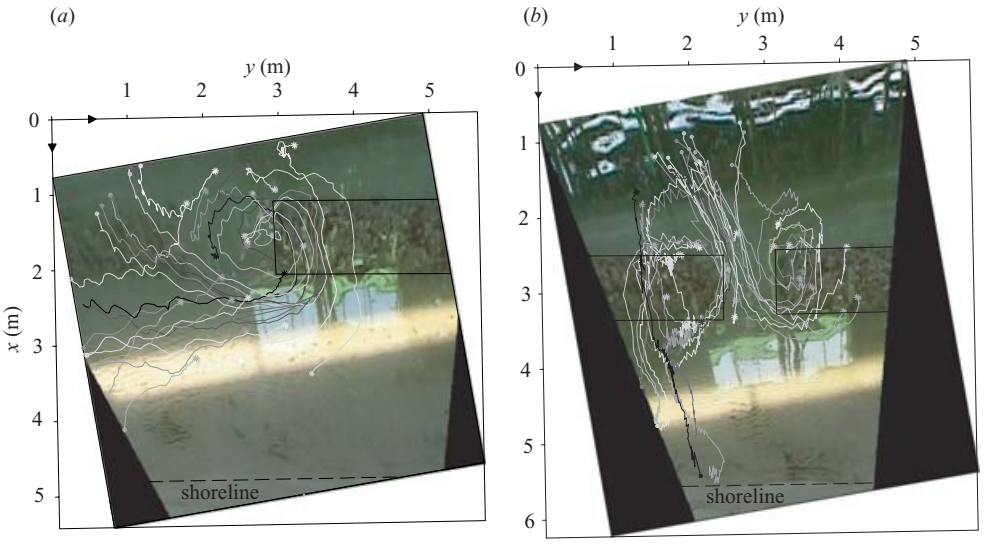


FIGURE 6. Examples of particles trajectories for the experimental cases: (*a*) single breakwater configuration (bari_v4_e1); (*b*) rip current configuration (bari_v2_f3). Stars represent the beginning of the trajectories and solid circles their end. The bright band crossing the images from left to right inshore of the breakwaters is due to unavoidable light reflection off the water surface.

locations of floaters were random but close to the gaps separating the central breakwater of figure 5 from the two lateral ones. Images, rectified into Cartesian still-water coordinates, allow inspection of the floaters' dispersion under the action of waves, currents and macrovortices (more details on the procedure can be found in Kennedy & Thomas (2004) and in Part 2). The location of each floater is characterized by an uncertainty due both to the raw data definition and to the image rectification procedure, the global result being an error in the range of 1–2 cm. For each test, tracking of floaters began at a zero time occurring prior the wave paddle starting its motion and lasting until the water became almost still after the paddle was stopped. Therefore, particles are first subjected to the small-scale turbulence field, then evolve because of the combined action of both larger-scale turbulence and waves, to reach a final stage when, far enough from the structures, they are weakly advected by macrovortices (of reduced intensity) and currents, thus mainly bobbing in the waves. Hence, as described in the following, because of floaters leaving the interrogation area, statistics could only be computed for 40–50 s after the waves reached the breakwaters.

A similar procedure was used for the single breakwater configuration but a different bathymetry had to be used because of problems in tracking the floaters when released around the leftmost structure of figure 3. Hence, an isolated breakwater was obtained by removing the leftmost and rightmost breakwaters of figure 5(*b*) and by running waves for a few hours until the quasi-steady bottom configuration of figure 5(*c*) was achieved before the tracers' analyses could start.

Figure 6 gives an example of the floaters meandering after being released in the channel between two breakwaters, i.e. rip current configuration (panel *b*) and in the vicinity of the single breakwater (panel *a*); from the latter a longshore drift current is evident of a few centimetres per second as reported in Lorenzoni *et al.* (2004) and also discussed in Part 2. There the dominance of longshore flows in the case of isolated structures is shown to largely depend on the relative size of the gap with

respect to the breakwater length ($L_t \gg L_c$) and for large enough beach/bar slopes ($|s_{beach} - s_{bar}| > h_b/L_c$). The presence of the rip current and its effects on the particles' dispersion are clearly shown in figure 6(*b*).

In particular it is clear that the rip current determines a strongly anisotropic field, with a cross-shore dispersion greater than the longshore one, especially in the rip neck. It is also possible to observe that the circulation cell is characterized by a size comparable with the breakwater length ($\sim 4$ m).

The experimental cases used for such analyses are summarized in table 3 and are characterized by configurations made up of either a single breakwater (v3, v4) or of an array of breakwaters (v2).

## 4. Statistical analysis of passive tracers trajectories

Flow mixing is quantified here in terms of absolute and relative statistics (i.e. dispersion and diffusivity) of experimental floaters' motion and the results are, in many ways, consistent with the predictions of the theory of two-dimensional flow mixing. On the other hand, some features specific to shallow flows forced by waves over topographic obstacles, like submerged breakwaters, have been highlighted.

In particular we analyse and discuss not only the behaviour in time of both the absolute and relative dispersion/diffusivity but also the dependence of the relative diffusivity on the length scale, i.e. the distance $D$. (Note that, for these mixing evaluations, the limits imposed by the available window size are such that floaters can be regarded as always residing in a region with intense wave-breaking-induced turbulence.)

The analysis of all the available data from the laboratory experiments suggests a simple scenario, characterized by three regimes: a 'microturbolence regime', an 'intermediate regime' and a final 'equilibrium regime'. We analyse the statistics underlying the different behaviours both of the different configurations (i.e. single breakwater configuration and rip current configuration) and of the different wave conditions (i.e. the dependence on the offshore wave height $H_0$ and period $T_0$).

We find that the results pertaining to all statistically equivalent cases are very similar, repeatability of their salient features being robust. Hence, for this reason and for the sake of clarity we only show results of representative cases to illustrate the dynamics. These representative cases are bari_v4_e1 and bari_v4_f3 respectively for short and long waves over a single breakwater; cases bari_v2_e2 and bari_v2_f3 are used for describing respectively short and long waves over an array of breakwaters.

### 4.1. *Absolute statistics*

The absolute statistics (diffusion and diffusivity) computed from the available data usually match well those of a 'ballistic regime' ($t < T_L$), a first regime, here called a 'microturbulence regime', which is characterized by a dispersion only caused by the microturbulence, the macroturbulence due to waves and large-scale eddies being absent. The analysis of the absolute dispersion $\langle X^2 \rangle$ for all floaters, both for the single breakwater configuration and rip current configuration shows the classical initial quadratic growth in time, representing the ballistic regime, till the time at which the waves reach the breakwaters ($t \approx 10$–$15$ s) (see figures 7 and 8, where the 68 % confidence limits are indicated by the bars). Using equation (2.4) we can compute the absolute diffusivity, as the time derivative of the absolute dispersion. As shown in figures 9 and 10, for all these cases the absolute diffusivity grows linearly in time, i.e. $K^{(1)} \propto t$ for $t < 10$–$15$ s.

| Cases | $H_0$ (cm) | $T_0$ (s) | $n_{in}$ | $t_{out}$ (s) | $n_{fin}$ | $n_{p1}$ | $n_{p2}$ | $n_{p3}$ |
|---|---|---|---|---|---|---|---|---|
| | | | Single breakwater configuration | | | | | |
| bari_v3_a1 | 1.67 | 0.9 | 26 | 95 | 23 | 40 | 119 | 228 |
| bari_v3_b1 | 1.67 | 1.8 | 24 | 80 | 21 | 44 | 117 | 205 |
| bari_v3_c1 | 3.33 | 0.9 | 26 | 90 | 22 | 30 | 93 | 198 |
| bari_v3_d1 | 3.33 | 1.8 | 25 | 60 | 17 | 20 | 58 | 120 |
| bari_v3_e1 | 5.00 | 0.9 | 26 | 80 | 13 | 9 | 30 | 63 |
| bari_v3_f1 | 5.00 | 1.8 | 26 | 40 | 13 | 15 | 25 | 56 |
| bari_v3_g1 | 6.67 | 0.9 | 20 | 30 | 16 | 14 | 58 | 109 |
| bari_v3_h1 | 6.67 | 1.8 | 24 | 40 | 18 | 25 | 64 | 136 |
| bari_v3_j1 | 5.00 | 1.8 | 26 | 50 | 15 | 25 | 51 | 102 |
| bari_v4_e1 | 5.00 | 0.9 | 28 | 59 | 20 | 18 | 64 | 153 |
| bari_v4_e2 | 5.00 | 0.9 | 25 | 76 | 19 | 26 | 66 | 151 |
| bari_v4_e3 | 5.00 | 0.9 | 26 | 70 | 17 | 24 | 49 | 93 |
| bari_v4_f1 | 5.00 | 1.8 | 22 | 54 | 15 | 24 | 54 | 96 |
| bari_v4_f2 | 5.00 | 1.8 | 24 | 50 | 18 | 26 | 75 | 152 |
| bari_v4_f3 | 5.00 | 1.8 | 25 | 50 | 18 | 41 | 60 | 130 |
| bari_v4_g1 | 6.67 | 0.9 | 26 | 55 | 18 | 18 | 41 | 109 |
| bari_v4_h1 | 6.67 | 1.8 | 26 | 50 | 20 | 34 | 85 | 173 |
| bari_v4_j1 | 5.00 | 1.8 | 23 | 40 | 13 | 13 | 34 | 72 |
| | | | Rip current configuration | | | | | |
| bari_v2_a1 | 1.67 | 0.9 | 24 | 100 | 22 | 26 | 98 | 199 |
| bari_v2_a2 | 1.67 | 0.9 | 25 | 100 | 24 | 26 | 93 | 219 |
| bari_v2_a3 | 1.67 | 0.9 | 24 | 120 | 22 | 14 | 70 | 164 |
| bari_v2_b1 | 1.67 | 1.8 | 25 | 170 | 16 | 9 | 30 | 70 |
| bari_v2_b2 | 1.67 | 1.8 | 23 | 170 | 9 | 5 | 14 | 33 |
| bari_v2_b3 | 1.67 | 1.8 | 22 | 170 | 12 | 4 | 17 | 38 |
| bari_v2_c1 | 3.33 | 0.9 | 24 | 120 | 22 | 19 | 80 | 196 |
| bari_v2_c2 | 3.33 | 0.9 | 22 | 107 | 16 | 8 | 41 | 102 |
| bari_v2_c3 | 3.33 | 0.9 | 23 | 100 | 18 | 34 | 88 | 147 |
| bari_v2_d1 | 3.33 | 1.8 | 25 | 80 | 19 | 21 | 68 | 146 |
| bari_v2_e1 | 5.00 | 0.9 | 25 | 90 | 20 | 23 | 88 | 156 |
| bari_v2_e2 | 5.00 | 0.9 | 25 | 72 | 20 | 37 | 105 | 178 |
| bari_v2_e3 | 5.00 | 0.9 | 24 | 72 | 17 | 27 | 77 | 128 |
| bari_v2_f1 | 5.00 | 1.8 | 22 | 40 | 19 | 22 | 70 | 153 |
| bari_v2_f2 | 5.00 | 1.8 | 25 | 45 | 20 | 19 | 70 | 143 |
| bari_v2_f3 | 5.00 | 1.8 | 24 | 45 | 18 | 37 | 78 | 134 |
| bari_v2_g1 | 6.67 | 1.8 | 24 | 45 | 20 | 17 | 56 | 132 |
| bari_v2_h1 | 6.67 | 1.8 | 23 | 45 | 16 | 8 | 32 | 87 |
| bari_v2_j1 | 5.00 | 1.8 | 25 | 45 | 18 | 33 | 91 | 148 |

TABLE 3. Main characteristics of the experimental cases performed at the University of Bari. $H_0$ and $T_0$ are the offshore wave height and period, $n_{in}$ is the total number of particles at $t = 0$ s, $t_{out}$ is the time for which a sufficient, for the statistical analysis, number of particles $n_{fin}$, are still in the domain, $n_{p1}$, $n_{p2}$ and $n_{p3}$ are the number of pairs for the three initial separations used for the relative dispersion analysis, i.e. for $D_0 = 0.4$ m, $D_0 = 0.8$ m and $D_0 = 1.5$ m respectively.

A second, intermediate regime, which we define as the 'growth regime', is observed for approximately 10–20 s $< t <$ 40–60 s. Figures 7/8 and 9/10 show that the duration of this regime is function both of the wave forcing and of the topographic features. As better clarified in the following section, in this regime the macroturbulence, induced by waves (single breakwater configuration) and large-scale shear (rip current configuration), dominates.

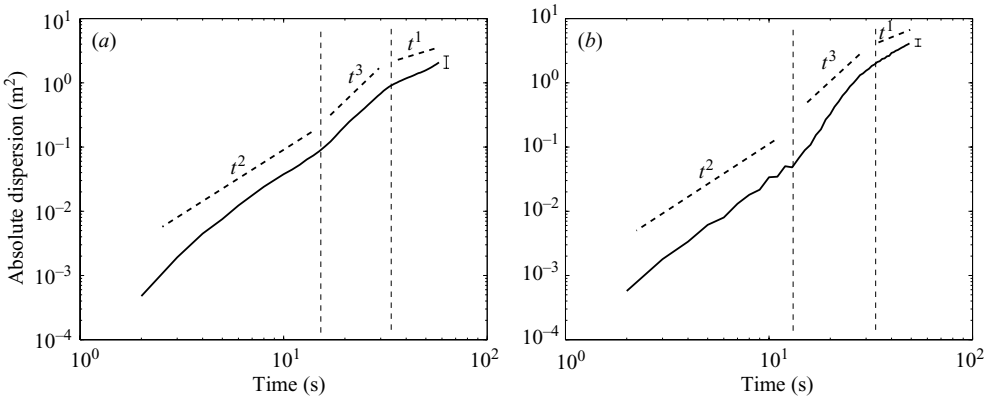


FIGURE 7. Absolute dispersion $\langle X^2 \rangle$ for the single breakwater configuration: (*a*) short wave (bari_v4_e1); (*b*) long wave (bari_v4_f3). The 68 % confidence limits are indicated by the bars.

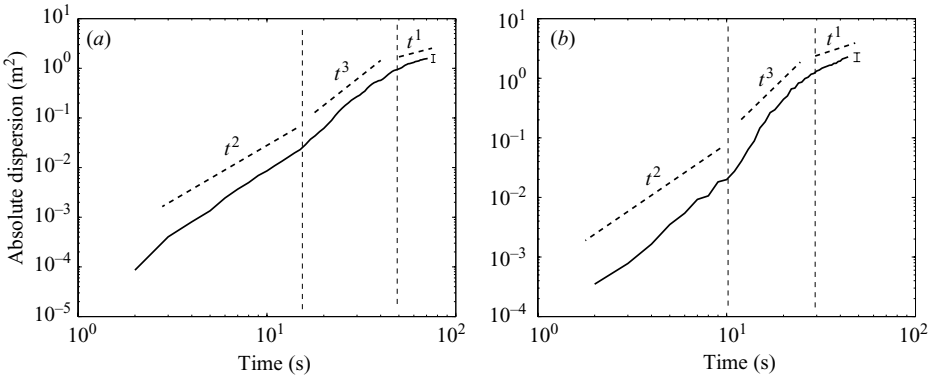


FIGURE 8. Absolute dispersion $\langle X^2 \rangle$ for the rip current configuration: (*a*) short wave (bari_v2_e3); (*b*) long wave (bari_v2_f3). The 68 % confidence limits are indicated by the bars.

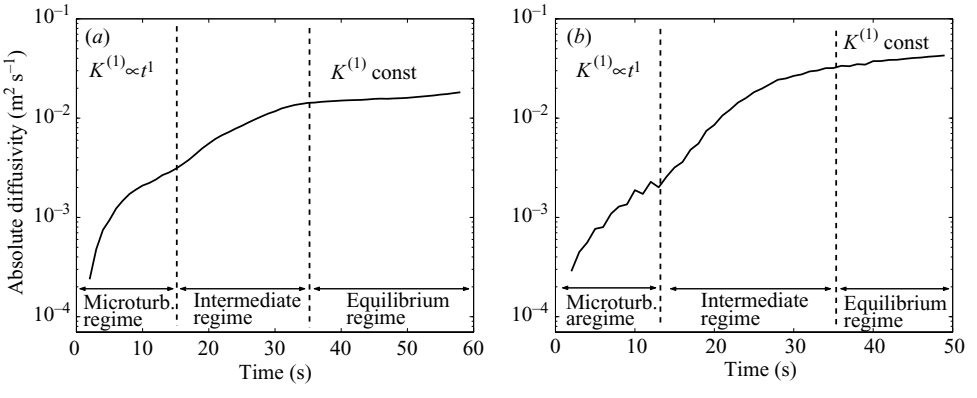


FIGURE 9. Absolute diffusivity $K^{(1)}$ for the single breakwater configuration: (*a*) short wave (bari_v4_e1); (*b*) long wave (bari_v4_f3).

Using the results both of the single breakwater configuration and of the rip current configuration, we have found that the growth regime is characterized by a $t^3$-power law, i.e. $\langle X^2 \rangle \propto t^3$ for the absolute dispersion (see figures 7 and 8). The time at

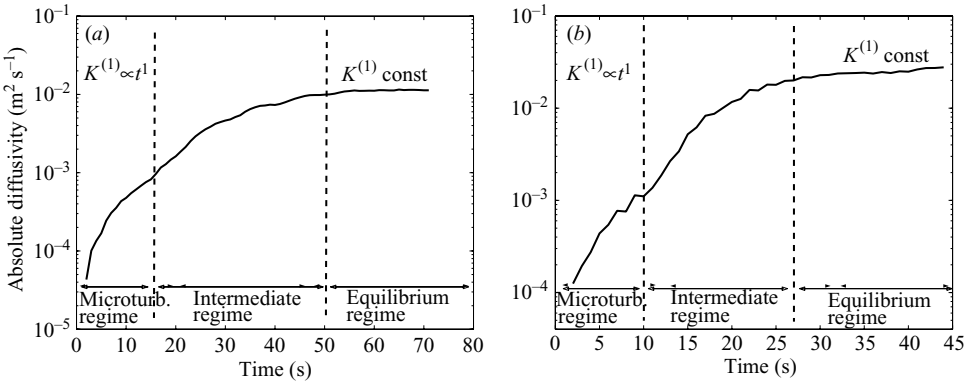


FIGURE 10. Absolute diffusivity $K^{(1)}$ for the rip current configuration: (*a*) short wave (bari_v2_e3); (*b*) long wave (bari_v2_f3).

which the transition between the intermediate and the final asymptotic phase occurs is around $t \approx 40$–$60$ s.

A final 'equilibrium regime' ($t > T_L$) is found in which the generation, transport and decay of the main large-scale features balance to give a sort of mean steady state. In this regime, reached after some decorrelation times, the absolute statistics behave as in the case of a Brownian regime. We, thus, find an almost linear growth of the absolute dispersion as shown by figures 7 and 8 and a constant value for the absolute diffusivity for large times as illustrated by figures 9 and 10. From a comparison between the results for the single breakwater configuration and for the rip current configuration, we can observe that the asymptotic value of the absolute dispersion $\langle X^2 \rangle$ for the single breakwater cases is greater than that of the rip current. This seems some first evidence that the rip current jets may reduce, owing to their spatial coherence, the dispersion of the floaters.

From a comparison among the behaviours of the absolute diffusivities due to the single breakwater configurations (see for example figure 9) we can conclude that for short waves (wave period $T = 0.9$ s), the absolute diffusivity, $K^{(1)} \approx (1.5$–$3.5) \times 10^{-2}\,m^2\,s^{-1}$, is smaller than that of long waves (wave period $T = 1.8$ s) for which $K^{(1)} \approx (2.9$–$5.7) \times 10^{-2}\,m^2\,s^{-1}$ (see table 4). This is also true for the rip current configurations (see for example figure 10) in which for short waves the values of absolute diffusivity are $K^{(1)} \approx (0.4$–$2) \times 10^{-2}\,m^2\,s^{-1}$ and for long waves $K^{(1)} \approx (0.7$–$4.8) \times 10^{-2}\,m^2\,s^{-1}$ (see table 4). The absolute diffusivity values are also directly proportional to the offshore wave height $H_0$. So the influence of the offshore wave height and period on the magnitude of the absolute diffusivity is clearly evident.

### 4.2. *Relative statistics*

The results illustrated in § 4.1 and the regime classification proposed there are given support and clarification on the basis of relative statistics.

Three initial separations are considered for the relative dispersion analysis, $D_0 = 0.4, 0.8, 1.5$ m, as shown in table 3. The smallest and the largest values are used to separate respectively the small- and large-scale turbulence. The intermediate value of $D_0$ is representative of the smallest gap width $L_t$. These scales have been chosen by taking into account both the information gained from the analysis of Part 2, for which $L_t$ is fundamental to assess the asymptotic flow regimes, and the need of adequately resolving the mixing. The latter requirement forces the use of

| Cases | $H_0^m$ (cm) | $T_0^m$ (s) | $H_0^p$ (m) | $T_0^p$ (s) | $K_m^{(1)}$ ($10^{-3}$ m$^2$ s$^{-1}$) | $K_p^{(1)}$ (m$^2$ s$^{-1}$) |
|---|---|---|---|---|---|---|
| Single breakwater configuration | | | | | | |
| bari_v3_a1 | 1.67 | 0.9 | 0.5 | 5 | 15.4 | 2.53 |
| bari_v3_b1 | 1.67 | 1.8 | 0.5 | 10 | 8.4 | 1.38 |
| bari_v3_c1 | 3.33 | 0.9 | 1.0 | 5 | 25 | 4.11 |
| bari_v3_d1 | 3.33 | 1.8 | 1.0 | 10 | 29 | 4.76 |
| bari_v3_e1 | 5.00 | 0.9 | 1.5 | 5 | 19 | 3.12 |
| bari_v3_f1 | 5.00 | 1.8 | 1.5 | 10 | 43 | 7.06 |
| bari_v3_g1 | 6.67 | 0.9 | 2.0 | 5 | 34 | 5.59 |
| bari_v3_h1 | 6.67 | 1.8 | 2.0 | 10 | 39 | 6.41 |
| bari_v3_j1 | 5.00 | 1.8 | 1.5 | 10 | 57 | 9.37 |
| bari_v4_e1 | 5.00 | 0.9 | 1.5 | 5 | 18 | 2.96 |
| bari_v4_e2 | 5.00 | 0.9 | 1.5 | 5 | 32 | 5.26 |
| bari_v4_e3 | 5.00 | 0.9 | 1.5 | 5 | 28 | 4.60 |
| bari_v4_f1 | 5.00 | 1.8 | 1.5 | 10 | 100 | 16.43 |
| bari_v4_f2 | 5.00 | 1.8 | 1.5 | 10 | 40 | 6.57 |
| bari_v4_f3 | 5.00 | 1.8 | 1.5 | 10 | 40 | 6.57 |
| bari_v4_g1 | 6.67 | 0.9 | 2.0 | 5 | 36 | 5.92 |
| bari_v4_h1 | 6.67 | 1.8 | 2.0 | 10 | 46 | 7.56 |
| bari_v4_j1 | 5.00 | 1.8 | 1.5 | 10 | 25 | 4.11 |
| Rip current configuration | | | | | | |
| bari_v2_a1 | 1.67 | 0.9 | 0.5 | 5 | 4.8 | 0.79 |
| bari_v2_a2 | 1.67 | 0.9 | 0.5 | 5 | 4.0 | 0.66 |
| bari_v2_a3 | 1.67 | 0.9 | 0.5 | 5 | 4.3 | 0.71 |
| bari_v2_b1 | 1.67 | 1.8 | 0.5 | 10 | 7.6 | 1.25 |
| bari_v2_b2 | 1.67 | 1.8 | 0.5 | 10 | 7.7 | 1.27 |
| bari_v2_b3 | 1.67 | 1.8 | 0.5 | 10 | 6.2 | 1.02 |
| bari_v2_c1 | 3.33 | 0.9 | 1.0 | 5 | 9.0 | 1.48 |
| bari_v2_c2 | 3.33 | 0.9 | 1.0 | 5 | 14.8 | 2.43 |
| bari_v2_c3 | 3.33 | 0.9 | 1.0 | 5 | 12.2 | 2.00 |
| bari_v2_d1 | 3.33 | 1.8 | 1.0 | 10 | 18.1 | 2.97 |
| bari_v2_e1 | 5.00 | 0.9 | 1.5 | 5 | 10.2 | 1.68 |
| bari_v2_e2 | 5.00 | 0.9 | 1.5 | 5 | 12.0 | 1.97 |
| bari_v2_e3 | 5.00 | 0.9 | 1.5 | 5 | 11.3 | 1.86 |
| bari_v2_f1 | 5.00 | 1.8 | 1.5 | 10 | 29.2 | 4.80 |
| bari_v2_f2 | 5.00 | 1.8 | 1.5 | 10 | 17.2 | 2.83 |
| bari_v2_f3 | 5.00 | 1.8 | 1.5 | 10 | 30.7 | 5.04 |
| bari_v2_g1 | 6.67 | 1.8 | 2.0 | 5 | 20.3 | 3.34 |
| bari_v2_h1 | 6.67 | 1.8 | 2.0 | 10 | 48.0 | 7.89 |
| bari_v2_j1 | 5.00 | 1.8 | 1.5 | 10 | 18.0 | 2.96 |

TABLE 4. Laboratory absolute diffusivity $K^{(1)}$ where superscripts $m$ and $p$ refer to the model and prototype scales, respectively.

relatively small values of separation, needed to resolve well the initial stages of the mixing (for this reason we neglect $L_c \sim 4.0$ m, close to the integral scale, as a suitable scale for the mixing analysis).

Different relative dispersion/diffusivity behaviours are found for the intermediate regime of the two configurations of single or neighbouring breakwaters. While for the latter both relative and absolute statistics are those typical of a shear-dominated flow, in the case of a single breakwater evidence has been found of an enstrophy cascade which, in principle, can be caused by either the stretching of vortex sheets from a shearing field (a qualitative example is shown in figure 11) or a merging of same-signed vortices.

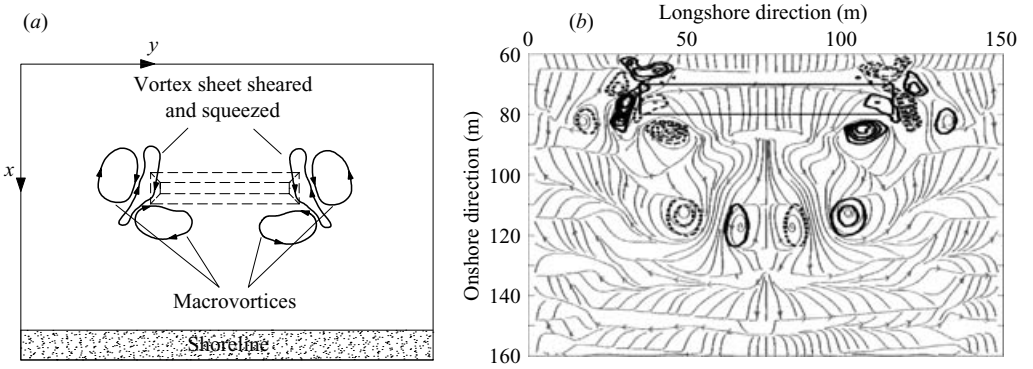


FIGURE 11. Qualitative example of the vortex stretching mechanism described by Kraichnan (1967) adapted to the flow of the single breakwater configuration: (*a*) simplified sketch; (*b*) results of NSWE numerical computations of Part 1 (see figure 3 of that paper). Solid contours represent positive (anticlockwise) vorticity, dashed contours negative (clockwise) vorticity.

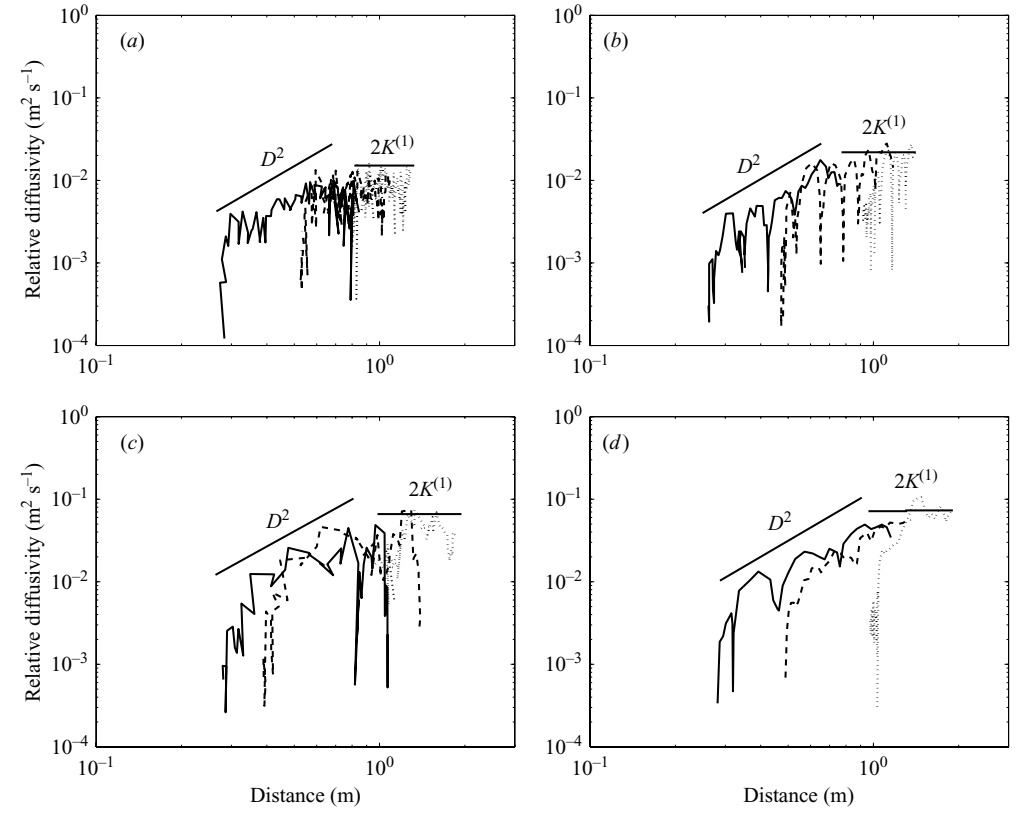


FIGURE 12. Single breakwater configuration. The relative diffusivity vs. mean separation distance for initial separations: $D_0 = 0.4$ m (solid line), $D_0 = 0.8$ m (dashed line) and $D_0 = 1.5$ m (dotted line). (*a*) bari_v3_b1, (*b*) bari_v4_e1, (*c*) bari_v4_f3, and (*d*) bari_v4_g1.

In figures 12 and 13 the total relative diffusivity, i.e. $K^{(2)} = K_x^{(2)} + K_y^{(2)}$, is plotted for the three initial separations $D_0 = 0.4, 0.8, 1.5$ m, against the distance $D$ defined as the square root of $\langle D^2 \rangle$. In agreement with the results of the relative dispersion for the scales of the intermediate regime ($D_0 < D < L_L$) the diffusivities exhibit a different

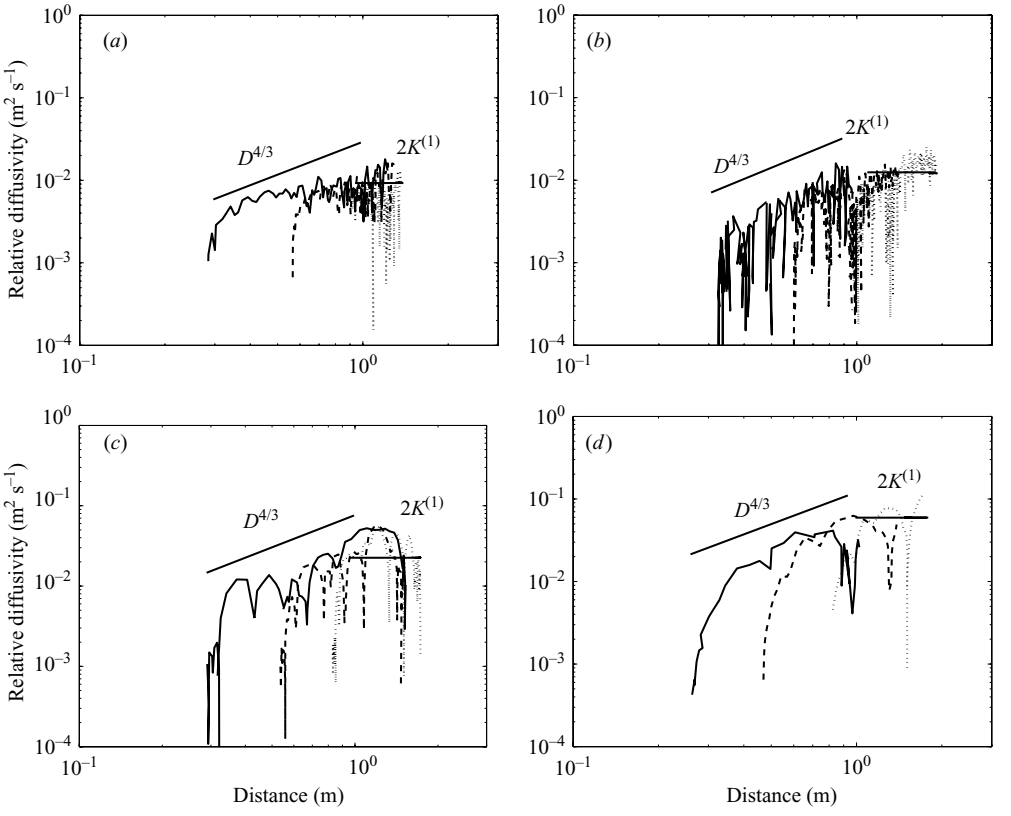


FIGURE 13. As figure 12 but fot the rip current configuration. (*a*) bari_v2_a1, (*b*) bari_v2_b3, (*c*) bari_v2_e3 and (*d*) bari_v2_f3.

power-law dependence for the single breakwater configuration (figure 12) and the rip current configuration (figure 13). The case of the single breakwater exhibits a $K^{(2)} \propto D^2$ law which seems to suggest an enstrophy cascade. On the contrary, the fit $K^{(2)} \propto D^{4/3}$ of figure 13 recalls the case of shear/waves dominance (Bennett 1987), rather than an inverse energy cascade, also in view of no evidence of vortex merging, which is essential for inverse energy cascading. Hence, the strong horizontal shear, given by the rip current, seems to cause the $D^{4/3}$-dependence for the relative diffusivity.

The flow anisotropy is analysed both in terms of absolute/relative dispersions, as shown in figure 14 (dotted lines indicate $\pm$ one standard deviation on the mean), and in terms of relative diffusivities in the $x$- and $y$-directions, as shown in figure 15. In particular for all the rip current configurations analysed (an example is shown in figure 15) the relative diffusivity in the cross-shore direction is greater than that in the longshore direction, $K_x^{(2)} > K_y^{(2)}$. We can also observe (see figure 14*b*) that for an array of submerged breakwaters the cross-shore relative dispersion $\langle D_{11}^2 \rangle$ is greater than the longshore component $\langle D_{22}^2 \rangle$, the cross-term $\langle D_{12}^2 \rangle$ being always small, while for the single breakwater configuration $\langle D_{11}^2 \rangle < \langle D_{22}^2 \rangle$. We can find a similar behaviour for the absolute dispersion in the $x$-direction $\langle X_{11}^2 \rangle$ and in the $y$-direction $\langle X_{22}^2 \rangle$. Absolute statistics also reveal that the mixing induced by the single breakwater configuration is significantly more anisotropic than that induced by the rip current configuration. These results, in agreement with the analyses of Part 2, show that the rip current

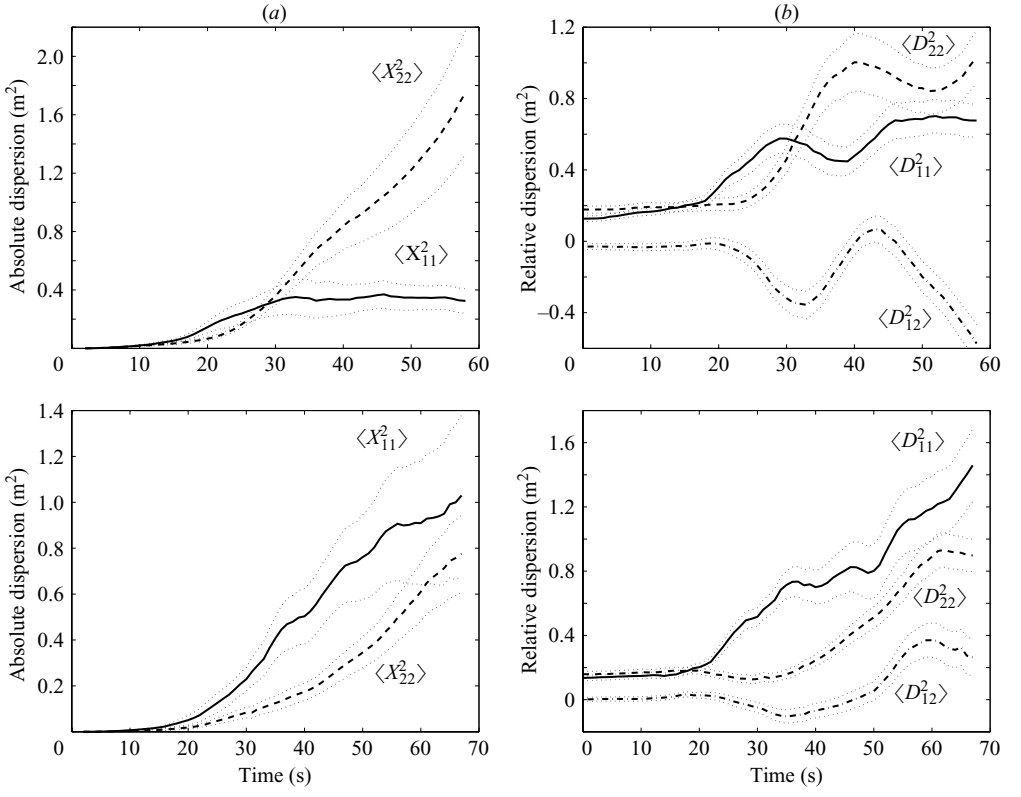


FIGURE 14. (*a*) The absolute and (*b*) relative dispersions in the *x*-direction (solid line), in the *y*-direction (dashed line) and the cross-term (dash-dotted line). Top: single breakwater configuration bari_v4_e1; bottom: rip current configuration bari_v2_e3. Dotted lines indicate $\pm$ one standard deviation on the mean.

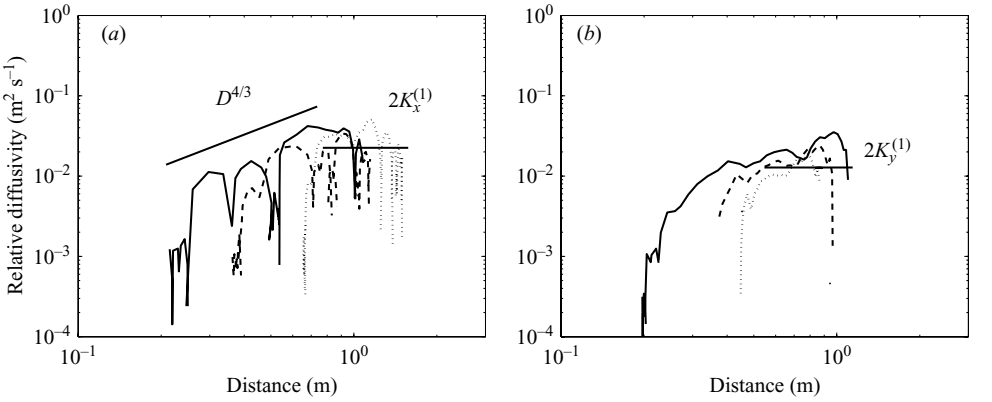


FIGURE 15. The relative diffusivity in (*a*) the *x*-direction $K_x^{(2)}$ and (*b*) the *y*-direction $K_y^{(2)}$ for the rip current configuration bari_v2_e3. For graphical arrangements see caption of figure 12.

configuration is dominated by a strong offshore and weak longshore transport while the single breakwater configuration is characterized by a strong longshore and weak cross-shore transport.

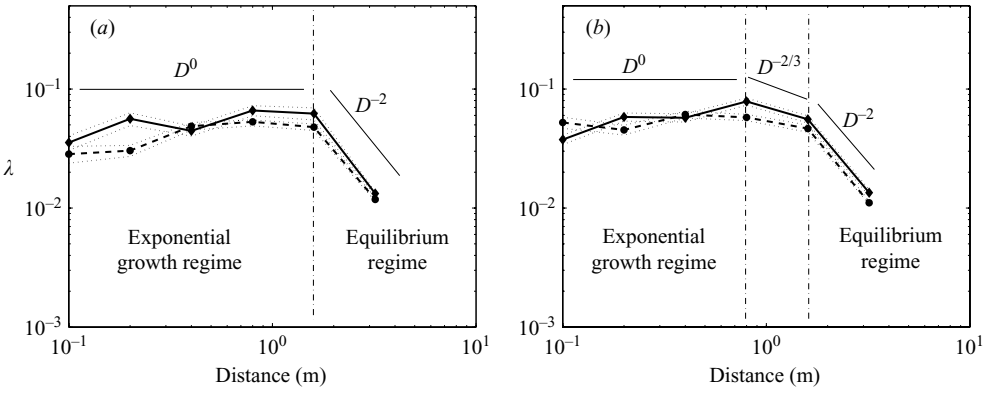


FIGURE 16. The finite-scale Lyapunov exponents FLSEs: (*a*) single breakwater configurations, bari_v4_e1 (dashed line) and bari_v4_f3 (solid line); (*b*): rip current configurations, bari_v2_e3 (dashed line) and bari_v2_f3 (solid line). The dotted lines indicate the 68 % confidence limits.

To better distinguish the relative dispersion behaviours, it is usual to introduce the 'characteristic time':

$$\tau(t) \equiv \frac{\langle D^2(t) \rangle}{K^{(2)}(t)}. \tag{4.1}$$

If this is constant, the growth rate of the relative dispersion may be represented by an exponential law typical of an enstrophy cascade regime (Babiano *et al.* 1990). This is often difficult to observe as, since it occurs in the intermediate regime, care must be taken in suitably choosing the initial separation $D_0$ which must be small enough with respect to the largest-scale eddies to adequately resolve the flow.

Beyond this limitation we also note that the unavoidable noise characterizing the relative diffusivity (see figures 12 and 13) can lead to problems of computation/interpretation of $\tau(t)$. We, thus, consider an alternative means of measuring dispersion, i.e. the finite scale Lyapunov exponents (FSLEs), in which the independent variable is a distance rather than a time (Aurell *et al.* 1997; LaCasce & Ohlmann 2003).

To calculate the FLSEs, choosing a set of pair separations $R_n$ increasing multiplicatively as

$$R_n = \alpha R_{n-1} = \alpha^n R_0 \tag{4.2}$$

in which $\alpha$ is a number greater than one, we calculate the times required for each pair's separation to grow to the successive $R_n$. The times are then averaged for each separation class. The maximum Lyapunov exponent, in the limit of small bin spacing, is given by

$$\lambda_s(n) = \ln(\alpha) \left\langle \frac{1}{T_n} \right\rangle. \tag{4.3}$$

It is important to note that the FLSE uses all sets of possible pairs. The FLSE behaviour is related to the relative dispersion growth rate. In particular, if the latter is represented by

$$\langle D^2 \rangle \propto t^n \qquad \text{the FSLE becomes} \qquad \left\langle \frac{1}{T_n} \right\rangle \propto D^{-2/n}. \tag{4.4}$$

In figure 16 we show the results in terms of the FLSE both for the single breakwater configuration (bari_v4_e1 and bari_v4_f3, panel *a*) and for the rip current configuration (bari_v2_e3 and bari_v2_f3, panel *b*). The dotted lines indicate the 68 % confidence

limits. Separations were calculated using $\alpha = 2$, but the results do not depend on this choice, which determines only the number of bins. We can observe that, for the single breakwater configuration, the mean inverse doubling time is almost constant (perhaps weakly increasing), i.e. $\lambda \sim 0.03\,\mathrm{s}$, with the distance for separations smaller than 1.5 m, which represents the case of exponential particle divergence; then the FLSE decreases like $D^{-2}$ which is consistent with a linear growth in the relative dispersion (i.e. the asymptotic regime characterized by standard diffusion). The results for the rip current configuration show a more complex scenario for the intermediate regime. An almost-constant dependence on $D$ ($\lambda \propto D^0$, rather $\lambda \sim 0.04\,\mathrm{s}$) is observed for separations smaller than about 0.8 m, then a weak decay $\lambda \propto D^{-2/3}$, not visible for the single breakwater configuration, is found for separations up to about 1.5 m. The latter regime is consistent with a growth of dispersion cubic in time and, consequently, with a $K^{(2)} \propto D^{4/3}$ regime. For separations larger than 1.5 m also the rip current configuration exhibits a $\lambda \propto D^{-2}$ decay which reflects an asymptotic or equilibrium regime.

The presence of an equilibrium regime is also clearly evident in all the reported results in terms of relative dispersion/diffusivity. For $D > L_L$ a linear growth in time of the relative dispersion is found which gives rise to a constant relative diffusivity $K^{(2)}$ about twice the absolute diffusivity $K^{(1)}$ for a distance larger than about 1 m. Note that horizontal line giving $2K^{(1)}$ in figures 12 and 13 is not just a reference but is computed from the available data. The 1 m size represents the Lagrangian scale $L_L$, i.e. the energy-containing scale, and compares well with the dimensions of the largest-scale eddies reported in Lorenzoni *et al.* (2004, 2005).

From a comparison between figures 12 and 13, we observe that the relative diffusivity for rip current configurations is approximately 2.5 times smaller than that characteristic of the single breakwater configurations; in particular, the former has mean values $K^{(2)} \sim 2K^{(1)} \approx (1.5\text{–}5.5) \times 10^{-2}\,\mathrm{m^2\,s^{-1}}$ while for the latter $K^{(2)} \sim 2K^{(1)} \approx (3.5\text{–}8.5) \times 10^{-2}\,\mathrm{m^2\,s^{-1}}$.

This quantitative result seems important in view of a general description of the mixing properties due to waves incident on either a single or an array of breakwaters and for use in practical computations of mixing using convective–diffusive equations like equation (1.1).

### 4.3. *Comparisons with field results*

We compare our experimental results with some recent and important field observations that Johnson & Pattiaratchi (2004) made for a rip current configuration. The comparison is performed in terms of the behaviour of the statistics and of the asymptotic values of relative diffusivity. The comparative analysis has two main aims. First of all we want to assess the validity of our assumption that scaled-down experiments can provide an adequate description of prototype conditions (present subsection). Hence, if the fundamental statistics, like the diffusivity, follow similar patterns to those found in the field we can expect scale effects to be negligible. In that case (see § 4.5), results from the Bari experiments can be used to prescribe relationships between flow conditions and $K^{(1)}$ to be used in practical applications.

Similarly to our experimental results (see § 3), Johnson & Pattiaratchi (2004) found that the diffusivity calculated both inside and outside the surf zone follows a 4/3-dependence, previously determined for oceanic turbulence at much larger scales (e.g. La Casce & Bower 2000).

Using a Froude similarity (clearly the best suited to a wave-dominated shallow flow), with a geometric scale ratio of 1:30, it is also possible to compare the values of relative diffusivities. In particular the relationships between length and time scales are

$L_m = L_p/30$ and $T_m = T_p/\sqrt{30}$ in which $L$ and $T$ represent length and time scales and the subscripts $m$ and $p$ represent 'model' and 'prototype', respectively. Using these relationships it is clear that

$$O(K_p) = O\left(\frac{L_p^2}{T_p}\right) = O\left[\left(\frac{L_m^2}{T_m}\right)\frac{30^2}{\sqrt{30}}\right] = 30\sqrt{30}K_m \tag{4.5}$$

which is used to compute the diffusivity at the prototype scale shown in table 4. The laboratory relative diffusivity $K^{(2)}$ is in the range $(0.8\text{–}3.6)\times 10^{-2}\,\mathrm{m^2\,s^{-1}}$ for the experimental cases with wave height comparable, at prototype scale, with that of the field experiments of Johnson & Pattiaratchi (2004); at prototype scale, the laboratory diffusivity values are equivalent to $K^{(2)} \approx 1.3\text{–}6\,\mathrm{m^2\,s^{-1}}$. The latter are similar, in order of magnitude, to the field relative diffusivity values reported by Johnson & Pattiaratchi (2004), ranging between 1.29 and $3.88\,\mathrm{m^2\,s^{-1}}$. However, these values are somewhat smaller than the order of magnitudes suggested by Inman *et al.* (1971) for both cross-shore and longshore diffusivities. In that work it was suggested that $O(K_x^{(2)}) = 10\,\mathrm{m^2\,s^{-1}}$ and that $O(K_y^{(2)}) = 100\,\mathrm{m^2\,s^{-1}}$. Hence, although this suggestion is in line with our observation that mixing dominated by longshore currents (our isolated breakwater) is more intense than that dominated by cross-shore currents (rip current configurations), the orders of magnitude suggested by Inman *et al.* (1971) seem more associated with intense events rather than average conditions. The linear scaling of $K_y^{(2)}$ with the separation between rip currents is also questionable. Such an assumption leads to too large values of diffusivity and a different scaling seems to give more reasonable results. Such a scaling is described in detail in the next subsection.

From the behaviour of the relative diffusivities in the $x$-direction and $y$-direction, shown in figure 15, it is possible to determine the values of the decorrelation length scales $L_x$ and $L_y$, for which the individual particles' velocities in the $x$- and $y$-directions are uncorrelated, respectively equal to $L_x \approx 0.6\text{–}1.2\,\mathrm{m}$ and $L_y \approx 0.5\text{–}0.8\,\mathrm{m}$. At the prototype scale these length scales are equal to $L_x \approx 20\text{–}35\,\mathrm{m}$ and $L_y \approx 15\text{–}25\,\mathrm{m}$, which show a good agreement with the field results for a rip current oriented normal to the shore (Johnson & Pattiaratchi 2004) of, respectively $L_x \approx 30\text{–}40\,\mathrm{m}$ and $L_y \approx 20\text{–}30\,\mathrm{m}$. The laboratory values slightly underestimate field ones, probably because of the spatial limitation of the experimental domain.

### 4.4. *Absolute diffusivity: parametric analysis*

The present results, in terms of the absolute diffusivity values, can also be used to determine relationships that have practical application for the computation of nearshore flow mixing. These are, usually, aimed at estimating the absolute diffusivity $K^{(1)}$ by means of general flow parameters. One of the formulae most frequently used is that of Larson & Kraus (1991) for which an estimate $K_*$ of $K^{(1)}$ is given, for a flow evolving over a planar beach, by

$$K_* = C_K u_b H \tag{4.6}$$

in which $C_K$ is a dimensionless constant experimentally determined as $C_K = 0.15\text{–}0.50$, $u_b$ is the local/representative bottom friction velocity and $H$ is the local/representative wave height.

We seek to obtain a similar relationship valid for a complex topography like that described in Part 1 and Part 2, in which the estimated value $K_*$ of the absolute diffusivity $K^{(1)}$ is

$$K_* = C_K \widetilde{U}\widetilde{L} = C_K\sqrt{g h_b} H_0. \tag{4.7}$$

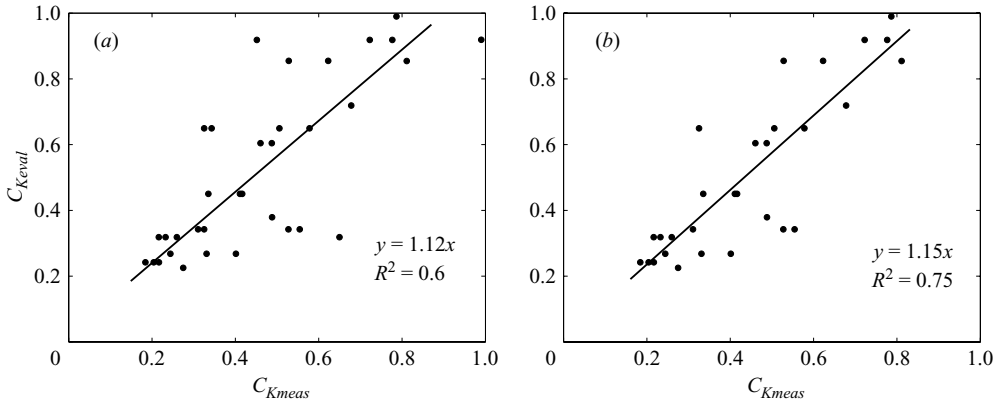


FIGURE 17. Comparison between the values of the dimensionless function $C_{Kmeas}$ determined by (4.10) from the experimental measures and the computed values of (4.9), reported along the $x$- and the $y$-axis respectively: (*a*) all experimental data; (*b*) best-fitting data.

Here the velocity scale $\widetilde{U}$ is taken as the local wave celerity $c = \sqrt{gh_b}$, with $h_b$ equal to the water depth at the offshore breakwater toe, and the length scale $\widetilde{L}$ is taken as the offshore wave height $H_0$. In order to account for topographic effects and wave propagation we do not take $C_K$ as a constant, but as a dimensionless function of the type

$$C_K = f(I_r, L_t/L_c) \tag{4.8}$$

in which $I_r \equiv s/\sqrt{H_0/L_0}$ is the Iribarren number, used to take account of the influence both of the wave period $T_0$ through the wavelength $L_0 = gT_0^2/(2\pi)$ and of the bottom slope $s$. Moreover, the function $C_K$ depends on the gap dimension $L_t$, whose asymptotic values $L_t \to 0$ and $L_t \to \infty$ respectively give the rip current configuration and the single breakwater configuration. As shown in Part 2 the geometry, and in particular the gap dimension, influence the circulation patterns, with different behaviour for the single breakwater configuration and the rip current configuration, respectively dominated by longshore and cross-shore flows. Hence the use of the breakwater length $L_c$ to make dimensionless $L_t$ and the dependence on the distance from the shoreline of the structures $x_b$, implicitly accounted for by using the bottom slope and the depth $h_b$ measured at the offshore toe of the breakwaters. Note that the breakwater submergence, kept constant to typical design values both here and in Parts 1 and 2, is also likely to influence $K_*$. However, in view of the available data and to keep the analysis as simple as possible, this dependence is disregarded here and its evaluation deferred to future studies.

In brief the proposed relationship is

$$C_K = 3.5\sqrt{I_r(L_t/L_c)} \Rightarrow K_* = 3.5\sqrt{I_r(L_t/L_c)}\sqrt{gh_b}H_0. \tag{4.9}$$

Using the experimentally measured values of the absolute diffusivity $K^{(1)}$, we compute the corresponding values of the dimensionless function $C_{Kmeas}$ as

$$C_{Kmeas} = K^{(1)}/(\sqrt{gh_b}H_0). \tag{4.10}$$

The geometric data used for the analysis are those of table 1 and the experimental values of the absolute diffusivity are reported in table 4.

A comparison between the values of the dimensionless function $C_{Kmeas}$ determined by (4.10) from the experimental measures and the values computed with (4.9) is shown in figure 17. In panel (*a*) we show the result obtained using all the experimental data

while panel (*b*) shows the best fitting. It is clear that, although with a relatively low correlation coefficient ($R^2 = 0.60$), the proposed relationship (4.9) represents all the experimental data well, the angular coefficient being 1.12. Removal of the data pertaining to irregular waves improves significantly the correlation coefficient ($R^2 = 0.75$), only moderately altering the angular coefficient which becomes 1.15.

Because of those results we believe that relationship (4.9) represents well the dependence of the absolute diffusivity $K^{(1)}$ both on the offshore wave height and period and on the different configurations, i.e. the single breakwater and the rip current configurations. However, predictions of (4.9) might worsen when using dimensionless parameters which differ too much from those here used.

Finally note that, owing to the limited fetches (100–300 m) of the coastal areas considered, wind stresses are here taken as having a negligible effect on the mixing. However, specific conditions may occur (e.g. strong winds flowing towards the offshore) for which wind-induced mixing could be as important as turbulence-induced mixing.

## 5. Conclusions

This work, the third in a series of studies on the nearshore dynamics due to breaking-wave-induced macrovortices, focuses on the mixing flow features. On the basis of laboratory experimental data the mixing of shallow flows occurring around submerged structures used for coastal protection is investigated in close analogy with that of two-dimensional flows. Analysis of particle statistics, both absolute and relative, suggests the flows of interest are characterized by three main regimes.

During the first stages of evolution, i.e. before the waves reach the breakwaters (microturbulence regime) an almost linearly growing absolute diffusivity $K^{(1)} \propto t$ characterizes a typical ballistic regime.

Once waves pass over the structures the flow turbulence is dominated, as also described in Part 2, either by waves and longshore mixing (single breakwater configuration) or by rip-induced shearing (rip current configuration). In this intermediate regime or growth regime relative statistics have distinct features that depend on the topography. In the case of isolated structures an exponential growth like $\langle D^2 \rangle \propto \exp(\beta^{1/3} t)$ characterizes the relative dispersion while the relative diffusivity undergoes a quadratic growth of the form $K^{(2)} \propto D^2$. Both results suggest an enstrophy cascade due to stretching of small-scale vortices by the action of the largest vortices generated at the breakwater edges. On the other hand, neighbouring breakwaters induce intense rip currents which dominate the flow behaviour. In fact a polynomial growth like $\langle D^2 \rangle \propto t^3$ characterizes the relative dispersion while the relative diffusivity grows like $K^{(2)} \propto D^{4/3}$. This 4/3-growth is similar to that recently found in the field in the case of rip currents (Johnson & Pattiaratchi, 2004).

A final regime characterizes the flow. In this equilibrium regime the flow features are similar to those of a typical Brownian regime and a constant relative diffusivity is found which approximately doubles the absolute diffusivity: $K^{(2)} \sim 2K^{(1)}$.

As well as this classification, which we found rather robust, other results important for practical applications have been obtained. It is clear that: (i) short waves induce smaller diffusivities than long waves, (ii) the large longshore dispersion induced by isolated structures forces a larger diffusivity than that due to rip currents: $K^{(1)}_{single} \sim (1.5\text{–}3.5) K^{(1)}_{rip}$.

An estimate $K_*$ has also been obtained for $K^{(1)}$ as function of the main wave $(H_0, L_0)$ and topographic features $(L_t, L_c, s, h_b)$

$$K_* = 3.5\sqrt{I_r(L_t/L_c)}\sqrt{gh_b}H_0 \tag{5.1}$$

which is proposed for use in nearshore water quality computations.

We thank A. Provenzale for the many useful discussions. We are grateful to C. Lorenzoni and L. Soldini for having made available the Bari data used in our analysis. The anonymous referees are thanked for a very insightful and useful review of our work. This research was partially supported within the MIUR PRIN 2003 Project 'Idrodinamica e morfodinamica di spiagge protette da opere tracimabili', under the grant number 2001082247–006.

## REFERENCES

Aurell, E., Boffetta, G., Crisanti, A., Paladin, G. & Vulpiani, A. 1997 Predictability in the large: an extension of the concept of Lyapunov exponent. *J. Phys.* A **30**, 1–26.

Babiano, A., Basdevant, C., Le Roy, P. & Sadourny, R. 1990 Relative dispersion in two-dimensional turbulence. *J. Fluid Mech.* **214**, 535–557.

Bennett, A. F. 1987 A Lagrangian analysis of turbulent diffusion. *Rev. Geophys.* **25**, 799–822.

Bowden, A. S. 1965 Horizontal mixing in the sea due to shearing current. *J. Fluid Mech.* **21**, 83–95.

Brocchini, M., Kennedy, A. B., Soldini, L. & Mancinelli, A. 2004 Topographically controlled, breaking-wave-induced macrovortices. Part 1. Widely separated breakwaters. *J. Fluid Mech.* **507**, 289–307.

Brocchini, M., Mancinelli, A., Soldini, L. & Bernetti, R. 2002 Structure-generated macrovortices and their evolution in very shallow depths. *Proc. 28th Intl Conf. Coast. Engng ASCE*, vol. 1, pp. 772–783.

Bühler, O. & Jacobson, T. E. 2001 Wave-driven currens and vortex dynamics on barred beaches. *J. Fluid Mech.* **449**, 313–339.

Chen, D. & Jirka, G. H. 1995 Experimental study of plane turbulent wake in a shallow water layer. *Fluid Dyn. Res.* **16**, 11–41.

Chen, Q., Dalrymple, R. A., Kirby, J. T., Kennedy, A. B. & Haller, M. C. 1999 Boussinesq modelling of a rip current system. *J. Geophys. Res.* **104**, 20617–20637.

Dracos, T., Giger, M. & Jirka, G. H. 1992 Plane turbulent jets in a bounded fluid layer. *J. Fluid Mech.* **241**, 587–614.

Dronen, N., Karunarathna, A., Fredsøe, J., Sumer, M. B. & Deigaard, R. 2002 An experimental study of rip channel flow. *Coast. Engng* **45**, 223–238.

Elhmaidi, D., Provenzale, A. & Babiano, A. 1993 Elementary topology of two-dimensional turbulence from a Lagrangian viewpoint and single-particle dispersion. *J. Fluid Mech.* **257**, 533–558.

Er-El, J. & Peskin, R. 1981 Relative diffusion of constant-level balloons in the Southern hemisphere. *J. Atmos. Sci.* **38**, 2264–2274.

Fong, D. A. & Stacey, M. T. 2003 Horizontal dispersion of a near-bed coastal plume. *J. Fluid Mech.* **489**, 239–267.

Haas, K. A. & Svendsen, I. A. 2002 Laboratory measurements of the vertical structure of rip currents. *J. Geophys. Res.* **107**, 3047.

Haller, M. C., Dalrymple, R. A. & Svendsen, I. A. 2002 Experimental study of nearshore dynamics on barred beach with rip channels. *J. Geophys. Res.* **107**, 3061.

Inman, D. L., Tait, R. J. & Nordstrom, C. E. 1971 Mixing in the surf zone. *J. Geophys. Res.* **76**, 3493–3514.

Johnson, D. & Pattiaratchi, C. 2004 Transient rip currents and nearshore circulation on swell dominated beach. *J. Geophys. Res.* **109**, doi:10.1029/2003JC001798.

Kennedy, A. B., Brocchini, M., Soldini, L. & Gutierrez, E. 2006 Topographically controlled, breaking-wave-induced macrovortices. Part 2. Rip current topographies. *J. Fluid Mech.* **559**, 57–80.

Kennedy, A. B. & Thomas, D. A. 2004 Drifter measurements in a laboratory rip current. *J. Geophys. Res. – Oceans* **109**, doi:10.1029/2003JC001982.

Kraichnan, R. H. 1967 Inertial ranges in two-dimensional turbulence. *Phys. Fluids* **10**, 1417–1423.

LaCasce, J. H. & Bower, A. 2000 Relative dispersion in the subsurface North Atlantic. *J. Mar. Res.* **58**, 863–894.

LaCasce, J. H. & Ohlmann, C. 2003 Relative dispersion in the surface of the Gulf of Mexico. *J. Mar. Res.* **61**, 285–312.

LaCasce, J. H. & Speer, K. 1999 Lagrangian statistics in unforced barotropic flows. *J. Mar. Res.* **57**, 245–275.

Larson, M. & Kraus, N. C. 1991 Numerical model of longshore current for bar and trough beaches. *J. Waterway, Port, Coast., Ocean Engng* **117**, 326–347.

Lippman, T. C. & Holman, R. A. 1989 Quantification of sand bar morphology: a video technique based on wave dissipation. *J. Geophys. Res. – Oceans* **94**, 995–1101.

Lorenzoni, C., Piattella, A., Soldini, L., Mancinelli, A. & Brocchini, M. 2005 An experimental investigation of the hydrodynamic circulation in the presence of submerged breakwaters. *Proc. 5th Intl Symp. Waves*, Paper 125.

Lorenzoni, C., Soldini, L., Mancinelli, A., Piattella, A. & Brocchini, M. 2004 La circolazione idrodinamica in presenza di barriere sommerse: un'analisi sperimentale. *Proc. XXIX Convegno di Idraulica e Costruzioni Idrauliche-Trento*, vol. 3, pp. 573–580 (in Italian).

Mancinelli, A., Soldini, L., Brocchini, M., Bernetti, R. & Scalas, P. 2001 Modelling the effects of structures on nearshore flows. *Proc. 4th Intl Symp. Waves*, pp. 1715–1724.

Morel, P. & Larcheveque, M. 1974 Relative dispersion of constant-level balloons in the 200 mb general circulation. *J. Atmos. Sci.* **31**, 2189–2196.

Oltman-Shay, J., Howd, P. A. & Berkemeier, W. A. 1989 Shear instabilities of the mean longshore current: field observations. *J. Geophys. Res. – Ocean* **94**, 18031–18042.

Peregrine, D. H. 1998 Surf zone currents. *Theoret. Comput. Fluid Dyn.* **10**, 295–309.

Pratt, L. J. 1983 On the inertial flow over topography. Part 1: semigeostrophic adjustment to an obstacle. *J. Fluid Mech.* **131**, 195–218.

Provenzale, A. 1999 Transport by coherent barotropic vortices. *Annu. Rev. Fluid Mech.* **31**, 55–93.

Richardson, L. F. 1926 Atmospheric diffusion shown on a distance neighbor graph. *Proc. R. Soc. Lond.* A **110**, 709–737.

Schär, C. & Smith, R. B. 1993 Shallow-water flow past isolated topography. Part I: vorticity production and wake formation. *J. Atmos. Sci.* **50**, 1373–1400.

Steijn, R., Roelvink, D., Rakhorst, D., Ribberink, J. & van Overeem, J. 1998 North Coast of Texel: a comparison between reality and prediction. *Proc. 26th Intl Conf. Coast. Engng, ASCE*, vol. 2, pp. 2281–2293.

Takewaka, S., Misaki, S. & Nakamura, T. 2003 Dye diffusion experiment in a longshore current field. *Coast. Engng. J.* **45**, 471–487.

Taylor, G. I. 1921 Diffusion by continuous movements. *Proc. Lond. Math. Soc.* **20**, 196–212.

Uijttewaal, W. S. J. & Booij, R. 2000 Effect of shallowness on the development of free-surface mixing layers. *Phys. Fluids* **12**, 392–402.